



Two Warm Super-Earths Transiting the Nearby M Dwarf TOI-2095

Elisa V. Quintana¹, Emily A. Gilbert², Thomas Barclay^{1,3}, Michele L. Silverstein^{1,3,35}, Joshua E. Schlieder¹, Ryan Cloutier⁴, Samuel N. Quinn⁵, Joseph E. Rodriguez⁶, Andrew Vanderburg⁷, Benjamin J. Hord^{1,8}, Dana R. Louie^{1,3,4}, Colby Ostberg⁹, Stephen R. Kane⁹, Kelsey Hoffman^{10,11}, Jason F. Rowe¹¹, Giada N. Arney¹, Prabal Saxena¹, Taran Richardson¹², Matthew S. Clement^{13,14}, Nicholas M. Kartvedt¹⁵, Fred C. Adams¹⁶, Marcus Alfred¹², Travis Berger¹, Allyson Bieryla⁵, Paul Bonney¹⁷, Patricia Boyd¹, Charles Cadieux¹⁸, Douglas Caldwell¹⁹, David R. Ciardi²⁰, David Charbonneau²¹, Karen A. Collins⁵, Knicole D. Colón¹, Dennis M. Conti²², Mario Di Sora²³, Shawn Domagal-Goldman¹, Jessie Dotson¹⁹, Thomas Fauchez¹, Erica J. Gonzales²⁴, Maximilian N. Günther²⁵, Christina Hedges^{1,3}, Giovanni Isopi²³, Erika Kohler¹, Ravi Kopparapu¹, Veselin B. Kostov¹, Jeffrey A. Larsen¹⁵, Eric Lopez¹, Franco Mallia²³, Avi Mandell¹, Susan E. Mullally²⁶, Rishi R. Paudel^{1,3}, Brian P. Powell¹, George R. Ricker⁷, Boris S. Safonov²⁷, Richard P. Schwarz²⁸, Ramotholo Sefako²⁹, Keivan G. Stassun^{30,31}, Robert Wilson¹, Joshua N. Winn³², and Roland K. Vanderspek³³

¹ NASA Goddard Space Flight Center, Greenbelt, MD 20771, USA; elisa.quintana@nasa.gov; michele.silverstein.ctr@nrl.navy.mil

² Jet Propulsion Laboratory, California Institute of Technology, Pasadena, CA 91109, USA

³ University of Maryland, Baltimore County, 1000 Hilltop Cir, Baltimore, MD 21250, USA

⁴ Department of Physics & Astronomy, McMaster University, 1280 Main St West, Hamilton, ON, L8S 4L8, Canada

⁵ Center for Astrophysics | Harvard & Smithsonian, 60 Garden St, Cambridge, MA, 02138, USA

⁶ Center for Data Intensive and Time Domain Astronomy, Department of Physics and Astronomy, Michigan State University, East Lansing, MI 48824, USA

⁷ Department of Physics and Kavli Institute for Astrophysics and Space Research, Massachusetts Institute of Technology, Cambridge, MA, 02139, USA

⁸ Astronomy Department, University of Maryland, College Park, MD 20742, USA

⁹ Department of Earth and Planetary Sciences, University of California, Riverside, CA 92521, USA

¹⁰ SETI Institute, 189 Bernardo Ave, Suite 200, Mountain View, CA 94043, USA

¹¹ Bishop's University, Department of Physics and Astronomy, 2600 College St, Sherbrooke, QC, J1M 1Z7, Canada

¹² Department of Physics and Astronomy, Howard University, 2400 6th St NW, Washington, DC 20059, USA

¹³ Johns Hopkins APL, 11100 Johns Hopkins Rd, Laurel, MD 20723, USA

¹⁴ Earth and Planets Laboratory, Carnegie Institution for Science, 5241 Broad Branch Rd, NW, Washington, DC 20015, USA

¹⁵ Department of Physics, United States Naval Academy, 572C Holloway Rd, Annapolis, MD 21402, USA

¹⁶ Department of Physics, University of Michigan, 450 Church St, Ann Arbor, MI 48109, USA

¹⁷ Department of Physics, University of Arkansas, 1 University of Arkansas, Fayetteville, AR 72701, USA

¹⁸ Université de Montréal, Département de Physique, IREX, Montréal, QC H3C 3J7, Canada

¹⁹ NASA Ames Research Center, Moffett Field, CA 94035, USA

²⁰ Caltech IPAC—NASA Exoplanet Science Institute 1200 E. California Ave, Pasadena, CA 91125, USA

²¹ Center for Astrophysics | Harvard & Smithsonian, 60 Garden St, Cambridge, MA 02138, USA

²² American Association of Variable Star Observers, 185 Alewife Brook Parkway, Suite 410, Cambridge, MA 02138, USA

²³ Campo Catino Astronomical Observatory, Regione Lazio, Guarcino (FR), I-03010 Italy

²⁴ Department of Astronomy and Astrophysics, University of California, Santa Cruz, CA 95064, USA

²⁵ European Space Agency (ESA), European Space Research and Technology Centre (ESTEC), Keplerlaan 1, 2201 AZ Noordwijk, The Netherlands

²⁶ Space Telescope Science Institute, 3700 San Martin Dr, Baltimore, MD, 21218, USA

²⁷ Sternberg Astronomical Institute, Lomonosov Moscow State University, 119992, Universitetskij prospekt 13, Moscow, Russia

²⁸ Center for Astrophysics | Harvard & Smithsonian, 60 Garden St, Cambridge, MA 02138, USA

²⁹ South African Astronomical Observatory, P.O. Box 9, Observatory, Cape Town 7935, South Africa

³⁰ Vanderbilt University, Department of Physics & Astronomy, 6301 Stevenson Center Ln, Nashville, TN 37235, USA

³¹ Fisk University, Department of Physics, 1000 18th Ave N, Nashville, TN 37208, USA

³² Department of Astrophysical Sciences, Princeton University, Princeton, NJ 08544, USA

³³ Department of Physics and Kavli Institute for Astrophysics and Space Research, Massachusetts Institute of Technology, Cambridge, MA 02139, USA

Received 2023 April 20; revised 2023 August 4; accepted 2023 August 18; published 2023 October 16

Abstract

We report the detection and validation of two planets orbiting TOI-2095 (TIC 235678745). The host star is a 3700 K M1V dwarf with a high proper motion. The star lies at a distance of 42 pc in a sparsely populated portion of the sky and is bright in the infrared ($K = 9$). With data from 24 sectors of observation during Cycles 2 and 4 of the Transiting Exoplanet Survey Satellite, TOI-2095 exhibits two sets of transits associated with super-Earth-sized planets. The planets have orbital periods of 17.7 days and 28.2 days and radii of $1.30 R_{\oplus}$ and $1.39 R_{\oplus}$, respectively. Archival data, preliminary follow-up observations, and vetting analyses support the planetary interpretation of the detected transit signals. The pair of planets have estimated equilibrium temperatures of approximately 400 K, with stellar insolutions of 3.23 and $1.73 S_{\oplus}$, placing them in the Venus zone. The planets also lie in a radius regime signaling the transition

³⁴ NASA Postdoctoral Program Fellow.

³⁵ Now resident at the U.S. Naval Research Laboratory as an NRC Research Associate.



between rock-dominated and volatile-rich compositions. They are thus prime targets for follow-up mass measurements to better understand the properties of warm, transition-radius planets. The relatively long orbital periods of these two planets provide crucial data that can help shed light on the processes that shape the composition of small planets orbiting M dwarfs.

Unified Astronomy Thesaurus concepts: [Exoplanets \(498\)](#); [M stars \(985\)](#)

1. Introduction

Among the most remarkable surprises revealed from large photometric transit surveys like Kepler/K2 (Borucki et al. 2010; Howell et al. 2014) and the Transiting Exoplanet Survey Satellite (TESS; Ricker et al. 2015) is that (1) the most abundant type of planets are those with sizes in-between that of Earth and Neptune ($1\text{--}4\times$ Earth’s radius, R_{\oplus}), and (2) the size distribution of this population appears to exhibit a bimodal feature, with a dearth of planets near $1.5\text{--}2\times R_{\oplus}$ for planets with orbital periods less than about 100 days (Owen & Wu 2013; Fulton et al. 2017; Van Eylen et al. 2018). The known planets smaller than Neptune, therefore, fall within two distinct populations: (1) enveloped terrestrial planets, or “super-Earths,” that are likely rocky, and (2) small planets with extended H/He envelopes, or “mini-Neptunes.” While the population analysis is primarily based on planets orbiting hotter stars, this bimodality has also been identified for exoplanets orbiting M dwarfs. However, in the case of M dwarfs, the center of the radius valley appears to shift to smaller planet sizes with decreasing stellar mass (Cloutier & Menou 2020), albeit not without controversy (Luque & Pallé 2022). There has since been a large body of research aimed at understanding what formation mechanisms drive these two populations, and whether there are separate formation paths for planets orbiting low-mass stars.

Several formation scenarios have been proposed to explain this bimodal distribution of the small exoplanet population. Because the aforementioned transit surveys are sensitive to planets orbiting close to their host stars (compared to the Earth-Sun system), the effect of the heating from the star may play a large role in the formation and retainment of exoplanet atmospheres, especially in relation to photoevaporation of atmospheres by high-energy (X-ray and extreme ultraviolet, XUV) radiation from the host star (Owen & Campos Estrada 2020). This degradation of the atmosphere due to incident stellar illumination and atmosphere loss driven by energy generated in the planet’s core (i.e., core-powered mass loss; Ginzburg et al. 2018) are mechanisms that may drive atmospheric escape on small exoplanets. The former is expected to occur early in the formation process, whereas the latter is expected to take place over billions of years (Cloutier & Menou 2020). Other scenarios that can explain the presence or lack of an atmosphere include accretion or erosion of atmospheric material during the tenuous impact phases of planet formation (Inamdar & Schlichting 2015), or the primordial presence and makeup of the gas component of protoplanetary disks while planets are forming (e.g., rocky planets may simply be born in a gas-poor or gas-depleted environment; Lopez & Rice 2018; Lee & Connors 2021)

Photoevaporation and core-powered mass loss are mechanisms that can explain atmosphere loss for planets orbiting low-mass stars only if their orbital periods are less than about 20–30 days (Cloutier & Menou 2020). Planets found on wider orbits are thus valuable to test the different proposed mechanisms that sculpt the radius valley. In particular, with follow-up mass (and

therefore composition) measurements, if planets on wider orbits are shown to be rocky, then we can deduce that they were likely formed that way.

Recently, Luque & Pallé (2022) have suggested that there are not two, but three populations of planets orbiting close to M dwarfs: rocky, water-rich, and gas-rich. They argue that planet bulk compositions are not driven by mass loss but rather by where the planets originally formed, such as rocky planets forming close to the ice line, and lower-density water worlds forming beyond the ice line and migrating inward. They see no evidence of any stellar insolation or orbital period dependence on the planet’s density which would be expected if the planetary composition was driven by mass loss. However, further research is needed to fully understand the origin and evolution of these types of planets (Rogers et al. 2023). Finding exoplanets that are amenable to mass measurements (which is the primary goal of TESS) will provide a way to test these theories, and help shed light on what truly shapes the compositions and atmospheres of small worlds.

Herein, we validate and characterize two planets orbiting the nearby M dwarf, TOI-2095, detected using TESS. The TOI-2095 system resides within the TESS and JWST continuous viewing zone (CVZ), and the host star is relatively bright (M1V) and quiet, making both planets excellent targets for obtaining follow-up precision radial velocity (mass) measurements. These planets have relatively long orbital periods (17.7 and 28.2 days), placing them in a regime where their atmospheres are less vulnerable to photoevaporation. Future mass measurements can therefore provide constraints on the formation and evolution processes that shape the composition of small planets orbiting M dwarfs.

2. TESS Observations

TOI-2095 is an M dwarf that resides in the Northern TESS Continuous Viewing Zone (CVZ), and Table 1 shows the specific observations taken by TESS. TOI-2095 was observed in all 13 sectors of Year 2 observations, including 12 sectors at 2 minute cadence (14–24 and 26), and all sectors in the 30 minute cadence full frame images (FFIs). In Year 4 of TESS operations, TOI-2095 was observed for 11 sectors (40, 41, and 47–55) in all cadences (20 s short cadence, 2 minutes short cadence, and 10 minutes FFIs). Observations of TOI-2095 continued in Cycle 5 for 6 sectors (Sectors 56–60, observed from 2022 August to 2023 January), but due to the availability of data during our analyses, these have not been included.

TOI-2095 was observed at higher cadence (2 minutes and 20 s cadence observing modes) as a result of its inclusion in a number of TESS Guest Investigator programs including G022198 (PI: Dressing, 2 minutes only) in Cycle 2 and G04006 (PI: Ramsay), G04039 (PI: Davenport), G04129 (PI: Buzasi), G04148 (PI: Robertson), G04178 (PI: Pepper), G04191 (PI: Burt), and G04242 (PI: Mayo) in Cycle 4. Both TOIs (TOI-2095.01 and TOI-2095.02) were alerted on 2020

Table 1
TOI-2095 Lies in the Northern Continuous Viewing Zone and was Observed by TESS in 29 Sectors Beginning 2019 July 18

Cycle	Sector	Camera	Cadence(s)	Cycle	Sector	Camera	Cadence(s)
2	14	3	2 min/FFI	4	47	4	2 min/FFI/20s
2	15	3	2 min/FFI	4	48	4	2 min/FFI/20 s
2	16	3	2 min/FFI	4	49	4	2 min/FFI/20 s
2	17	4	2 min/FFI	4	50	4	2 min/FFI/20 s
2	18	4	2 min/FFI	4	51	4	2 min/FFI/20 s
2	19	4	2 min/FFI	4	52	3	2 min/FFI/20 s
2	20	4	2 min/FFI	4	53	3	2 min/FFI/20 s
2	21	4	2 min/FFI	4	54	4	2 min/FFI/20 s
2	22	4	2 min/FFI	4	55	4	2 min/FFI/20 s
2	23	4	2 min/FFI	5	56	4	...
2	24	3	2 min/FFI	5	57	4	...
2	25	3	FFI	5	58	4	...
2	26	3	2 min/FFI	5	59	4	...
4	40	3	2 min/FFI/20 s	5	60	4	...
4	41	3	2 min/FFI/20 s				

Note. The analysis presented herein includes data from Cycle 2 to Cycle 4.

July 15 by TESS (Guerrero et al. 2021) following detection by the TESS pipeline (Jenkins et al. 2016). It was at this time that we began investigating this planetary system further.

3. Stellar Characterization

TOI-2095 is a low-mass star in the constellation of Draco. It was identified as a cool dwarf in the TESS Input Catalog (TIC; Muirhead et al. 2018; Stassun et al. 2019). We collated archival data on this source and combined the TIC information with newly collected data to derive stellar properties using multiple different approaches.

We used Gaia astrometric and radial velocity (RV) data from Data Release 3 (DR3, Gaia Collaboration et al. 2016, 2023). The astrometry and RV values were combined to determine the Galactic kinematics, presented in Table 2.

Photometric brightness values reported in Table 2 were drawn from Gaia Data Release 3 (DR3), the TIC, the Two Micron All-Sky Survey (2MASS; Cutri et al. 2003; Skrutskie et al. 2006), and the Wide-field Infrared Survey Explorer (WISE) AllWISE data release (Wright et al. 2010; Cutri et al. 2021). Using the Pecaut & Mamajek (2013) color-temperature table³⁶ and the available photometry, we estimated a spectral type of M1V.

We use multiple different approaches to estimate stellar parameters to allow cross-comparison and identify any outliers from the choice of parameter estimation method. Mass, radius, effective temperature, and luminosity are calculated using relations presented in Mann et al. (2015), Benedict et al. (2016), Mann et al. (2019), and an expanded version of the method presented in Dieterich et al. (2014) from Silverstein (2019). We estimate the stellar metallicity using the relations from Kesseli et al. (2019). When the parameter estimation approach requires absolute magnitudes, we use the most recent TOI-2095 parallax from Gaia DR3 (Gaia Collaboration et al. 2016, 2023).

Following the mass- M_K relation of Mann et al. (2019), we derived a mass of $0.465 \pm 0.012 M_\odot$. For this calculation, we computed M_K using the 2MASS K_s magnitude and Gaia DR3

parallax and adopted the Kesseli et al. (2019) metallicity, $[\text{Fe}/\text{H}] = -0.45 \pm 0.38$ dex. We found only a $0.001 M_\odot$ difference in the mass result when $[\text{Fe}/\text{H}] = 0$ dex was adopted. For comparison, we also calculate masses using the Benedict et al. (2016) mass- M_K and mass- M_V relations, which do not include a correction for metallicity. In agreement with the systematic comparison of the two relations in Mann et al. (2019), the M_K mass value of $0.518 \pm 0.020 M_\odot$ from the Benedict et al. (2016) relation is higher than that from the Mann et al. (2019) relation. Mann et al. (2019) note that the difference in the two mass- M_K relations likely stems from improvements in the observations of stars with masses $\gtrsim 0.35 M_\odot$ used to calibrate each method. We also derive a Benedict et al. (2016) mass- M_V relation value of $0.489 \pm 0.021 M_\odot$, with M_V calculated using a Gaia DR3 parallax and a V magnitude calculated using the Gaia DR3 photometry and conversions via the Riello et al. (2021) relations. This value matches the Benedict et al. (2016) mass- M_K result within the uncertainties.

We use the M_K relations in Mann et al. (2015) to estimate the luminosity, effective temperature, and radius. These calculations use a semi-empirical approach to parameter estimation calibrated with a sample of M dwarfs having interferometric radius measurements and also take into account the Kesseli et al. 2019 metallicity. The estimated values are provided in Table 3.

We also derived effective temperature, luminosity, and radius following the method described in Silverstein (2019), which is similar to that described in Dieterich et al. (2014). We compared observed VRI , 2MASS JHK_s , and WISE W1W2W3 photometry to photometry extracted from the BT-Settl 2011 photospheric models (Allard et al. 2012) to determine an effective temperature. Observational VRI were derived according to the Gaia DR2 photometry conversion. The closest-matching model spectrum to our T_{eff} was iteratively scaled by a polynomial until observations match the scaled model. The spectrum was then integrated within the wavelength range of the observations. A bolometric correction was applied based on how much blackbody flux would be missing beyond the observed wavelength range for a star of the same T_{eff} . Bolometric flux was then scaled by the Gaia DR3 parallax to produce bolometric luminosity. Lastly, effective temperature

³⁶ http://www.pas.rochester.edu/~emamajek/EEM_dwarf_UBVIJHK_colors_Teff.txt

Table 2
Host Star Observed Properties and Literature Values

Property	Value	Error	References
Identifiers	TOI-2095, TIC 235678745, Gaia DR2 2268372099615724288		
Astrometry and Kinematics			
R.A. J2016 (deg)	285.63663592007	0.0000000036	Gaia DR3
Decl. J2016 (deg)	+75.41851051257	0.0000000035	Gaia DR3
Parallax (mas)	23.8571	0.0133	Gaia DR3
Distance (pc)	41.917	0.023	Gaia DR3
R.A. Proper Motion (mas yr ⁻¹)	203.466	0.018	Gaia DR3
Decl. Proper Motion (mas yr ⁻¹)	-21.401	0.017	Gaia DR3
Radial Velocity (km s ⁻¹)	-19.94	0.52	Gaia DR3
U_{LSR} (km s ⁻¹)	5.95	0.32	This work
V_{LSR} (km s ⁻¹)	12.05	0.62	This work
W_{LSR} (km s ⁻¹)	-38.70	0.34	This work
Total Galactic Motion (km s ⁻¹)	40.97	0.37	This work
Photometry			
BP	12.086019	0.002779	Gaia DR3
RP	13.111851	0.003183	Gaia DR3
G	11.080335	0.003842	Gaia DR3
V_J	12.854	0.030	Gaia DR3 Conversion
V_J	12.838	0.046	Gaia DR2 Conversion
R_{KC}	11.870	0.032	Gaia DR3 Conversion
I_{KC}	10.934	0.038	Gaia DR3 Conversion
T	11.0788	0.0073	TICv8.1
J	9.797	0.020	2MASS
H	9.186	0.015	2MASS
K_s	8.988	0.015	2MASS
W1	8.868	0.025	AllWISE
W2	8.766	0.024	AllWISE
W3	8.670	0.024	AllWISE
W4	8.709	0.269	AllWISE
Spectral Features			
Spectral Type	M0.5V–M1.0V	...	Pecaut & Mamajek (2013) Table [*]
Metallicity ([Fe/H]; dex)	subsolar	...	This work: HR Diagram, SED Fits, etc.
	-0.45	0.38	Kesseli et al. (2019) relation

Note. 2MASS: Cutri et al. (2003); Skrutskie et al. (2006), WISE AllWISE Release: Wright et al. (2010); Cutri et al. (2021) (see footnote 36).

Table 3
Host Star Derived Properties (with Adopted Values in Bold)

Property	Value	Error	References
Names	TOI-2095, TIC 235678745, Gaia DR2 2268372099615724288		
Mass (M_{\odot})	0.465	0.012	Mann et al. (2019) Relation ([Fe/H]=-0.45)
	0.518	0.020	Benedict et al. (2016) \mathcal{M}_K Relation
	0.489	0.021	Benedict et al. (2016) \mathcal{M}_V Relation ^a
Effective Temperature (K)	3662	130	Mann et al. (2015) Relation ([Fe/H] = -0.45)
	3690	50	Silverstein (2019) ([Fe/H] = -0.5)
Luminosity (L_{\odot})	0.0333	0.0019	Mann et al. (2015) Relation ([Fe/H] = -0.45)
	0.0345	0.0008	Silverstein (2019) ([Fe/H] = -0.5)
Radius (R_{\odot})	0.453	0.029	Mann et al. (2015) Relation ([Fe/H] = -0.45)
	0.454	0.014	Silverstein 2019 ([Fe/H] = -0.5)
Density (g cm ⁻³)	7.05	1.38	Using Mann et al. M & R

Note.

^a Using a V magnitude converted from Gaia DR3 photometry.

and luminosity were substituted into the Stefan-Boltzmann law to calculate the stellar radius.

Using this method, we derived two sets of values for different adopted model metallicities, [Fe/H] = 0 dex and

[Fe/H] = -0.5 dex. We compared these results to those derived using the Mann et al. (2015) relations, which also include a metallicity term. We found that the results were a better match when both methods adopted a [Fe/H] value of

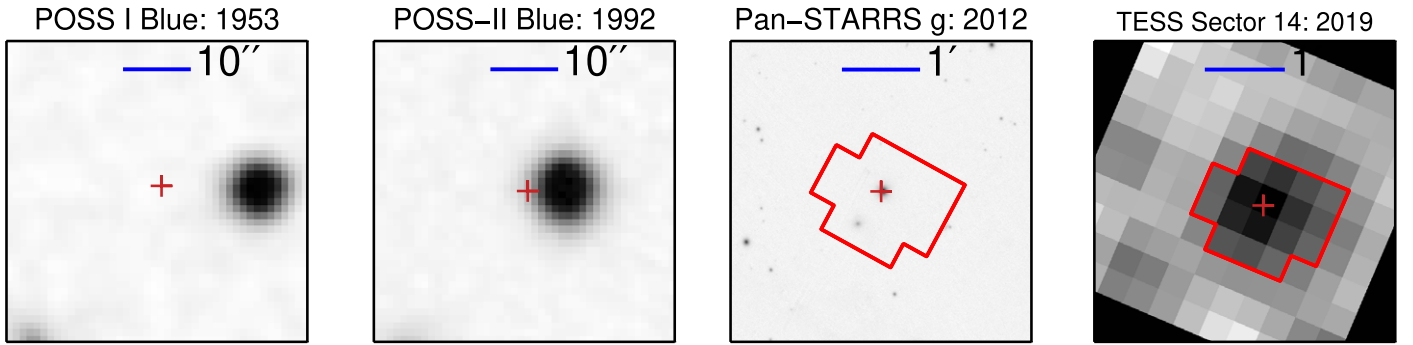


Figure 1. Archival imaging of TOI-2095. From left to right, an image from the first Palomar Observatory Sky Survey (POSS-I) in a blue-sensitive emulsion, an image from the second Palomar Observatory Sky Survey (POSS-II) in a blue-sensitive emulsion, an image from the Panoramic Survey Telescope and Rapid Response System (PAN-STARRS) telescope in g -band, and the summed image from TESS during Sector 14. The present-day position of TOI-2095 is shown with a red cross, and in the Pan-STARRS and TESS images, the outline of the TESS photometric aperture from Sector 14 is shown as a solid red line. TOI 2095’s high proper motion reveals no background sources at its present-day position that could give rise to the transits we see.

–0.5 dex, with T_{eff} and radius values nearly identical. Derived stellar properties are reported in Table 3. We adopt the Mann et al. (2015) and Mann et al. (2019) values for subsequent analyses in this paper due to their more conservative uncertainties which take into account the scatter in the calibration samples used in those relations.

TOI-2095 is likely slightly older and metal-poor compared to other M dwarfs of its spectral type. When plotted using Gaia DR3 photometry and astrometry, the star is relatively low on the color–magnitude diagram, common for lower-metallicity stars. A lack of starspot-induced photometric modulation and flares indicates low magnetic activity, more commonly seen in older stars. As described previously, agreement between methods to derive fundamental properties improves when subsolar metallicity is adopted. Photometric metallicities also suggest that the star is slightly metal-poor (Table 2). The total Galactic space motion of $\sim 41 \text{ km s}^{-1}$ does not suggest that the star is a member of the thick disk or Galactic halo.

4. Ground-based Observations for System Validation

In addition to observations from TESS, we collected numerous additional data sets in support of determining whether the two planetary transit signals are from bona fide planets. These data comprise high-contrast imaging, spectroscopy of the star, and photometry of the star collected during transits.

4.1. Imaging

TOI-2095 has large proper motion ($205.6 \text{ mas yr}^{-1}$) and has moved significantly since the first archival sky survey observations in the 1950s (see Figure 1). Within the ~ 5 pixel TESS aperture ($\sim 105''$ box) there are no background stars at the current location of TOI-2095 down to the background limits of the POSS-I surveys (~ 20 mag in B and R). There are 2 faint background galaxies within the aperture, but these cannot contribute as a source of false positives for the TESS detected transits.

High-contrast imaging enables us to infer limits on the brightness and separations of any bound, co-moving companions. To do so, we collected data using adaptive optics (AO) and speckle imaging techniques.

The limiting case is for a background totally eclipsing binary (i.e., a decrease in brightness by 50%; Barclay et al. 2013) If such a star were in the background of TOI-2095 then the total

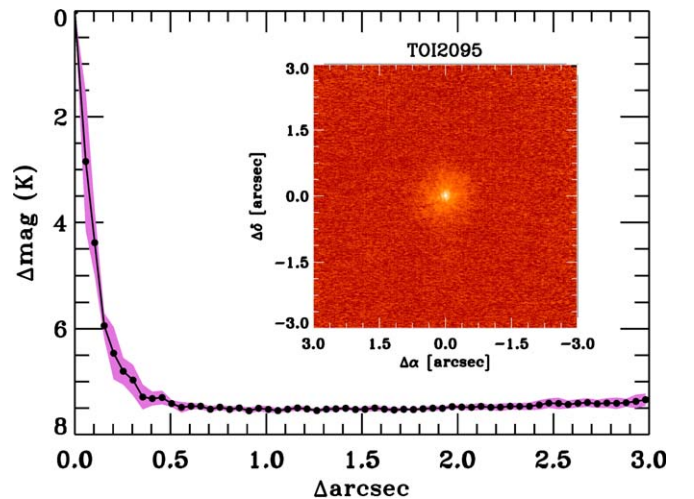


Figure 2. Keck II NIRC2 K -band adaptive optics image of TOI-2095 (inset) and contrast curve. No faint companions were detected down to 6 mag of contrast at separations of $0''.2$ and $7''.5$ mag at separations $>0''.5$

eclipse would need to be diluted to reach the observed depths of 0.8 mmag and 0.9 mmag for planets b and c , respectively. This is a dilution by factors 550 and 650, or approximately 7 mag. Therefore, the background eclipsing binary could be no fainter than $\text{TESSmag} = 18.1$ mag, 7 mag fainter than TOI-2095. The POSS-I plates are sensitive to about $R \sim 20$ mag and would have detected such a star. Additionally, the fact that TOI-2095 has two transiting planets yields a multiplicity boost to the statistical validation of the system (Lissauer et al. 2012; Rowe et al. 2014) with an estimated $\sim 2\%$ chance of a two-planet system being a false positive.

4.1.1. AO Imaging

We used the NIRC2 instrument behind the Natural Guide Star (NGS) AO system (Wizinowich et al. 2000) on the 10 m Keck II telescope. We obtained data on 2020 September 9 UT in the K -band filter with $\lambda_c = 2.196 \mu\text{m}$ and bandwidth $0.336 \mu\text{m}$ under clear skies. We followed the general observation plan and analysis approach described in Schlieder et al. (2021) for NIRC2 high-resolution imaging of TESS systems. Briefly, we observed using 0.181 s integrations following a standard dither sequence comprised of $3''$ steps that were repeated three times, with each subsequent dither offset $0''.5$. At

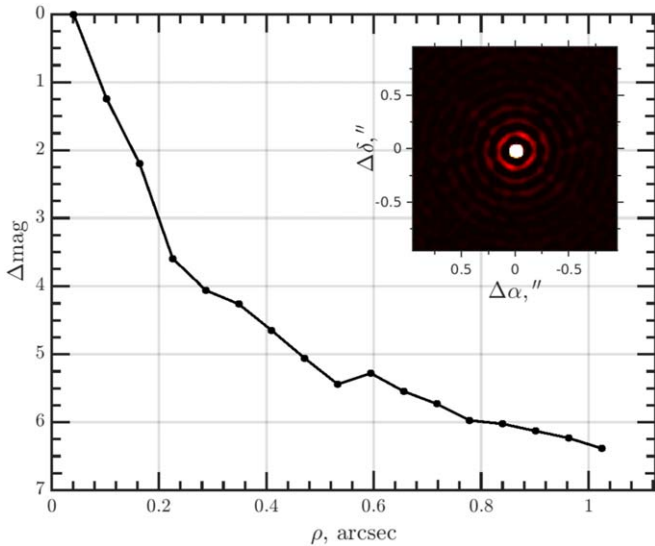


Figure 3. Speckle SAI image of TOI-2095 (inset) and contrast curve.

each location we used 1 co-add, resulting in 9 total frames. We used the narrow-angle mode of the NIRC2 camera which has a plate scale of $9.942 \text{ mas pixel}^{-1}$ and a $10''$ FOV. No companions were detected down to a contrast of 6 magnitudes at $0''.2$ (8.4 au separation at the distance of TOI-2095). At that contrast, the speckle I -band imaging was sensitive to stars to approximately mid-way through the M-dwarf sequence (M4–M5V; Pecauc & Mamajek 2013).

4.2. Speckle Imaging

TOI-2095 was observed on 2020 December 26 UT with the Speckle Polarimeter (Safonov et al. 2017) on the 2.5 m telescope at the Caucasian Observatory of Sternberg Astronomical Institute (SAI) of Lomonosov Moscow State University. SPP uses Electron Multiplying CCD Andor iXon 897 as a detector. The atmospheric dispersion compensator allowed observation of this relatively faint target through the wide-band I_c filter. The power spectrum was estimated from 4000 frames with 30 ms exposure. The detector has a pixel scale of $20.6 \text{ mas pixel}^{-1}$, and the angular resolution was 89 mas . We did not detect any stellar companions brighter than $\Delta I_C = 3.8$ and 6.4 at $\rho = 0''.25$ and $1''.0$, respectively, where ρ is the separation between the source and the potential companion, see Figure 3. At that contrast, the speckle I -band imaging was sensitive to stars to approximately mid-way through the M-dwarf sequence (M4–M5V; Pecauc & Mamajek 2013).

4.3. Additional Photometry

The TESS pixel scale is $\sim 21'' \text{ pixel}^{-1}$ and photometric apertures typically extend out to roughly $1'$, generally causing multiple stars to blend in the TESS aperture. To attempt to determine the true source of the detections in the TESS data and refine their ephemerides and transit shapes, we collected ground-based photometric follow-up observations of the field around TOI-2095 as part of the TESS Follow-up Observing Program³⁷ Subgroup 1 (TFOP; Collins 2019). We used the TESS Transit Finder, which is a customized version of the Tapir software package (Jensen 2013), to schedule our

transit observations. Differential photometric data were extracted using *AstroImageJ* (Collins et al. 2017).

Observations were collected during the transit of TOI-2095 b on 2020 September 23 UT from Campo Catino Rodeo Observatory in Rodeo, New Mexico using a remotely operated Planewave 35 cm telescope. The observations used a clear filter and 180 s exposures. This observation consists of seeing limited photometry of the system and the surrounding stars in order to check for nearby eclipsing binaries (NEB), following the standard TESS Follow-up Program (TFOP) Subgroup 1 (SG1) procedure.

The target light curve was flat with a scatter of 0.77 ppt with a 530 s cadence using a $13 \text{ px} = 5''.3$ aperture. This was close to the predicted depth (0.79 ppt), but no significant transit ingress was visible. An NEB check was performed using a $5 \text{ px} = 2''.5$ aperture and did not find any obvious NEBs.

A second epoch of NEB checking for TOI-2095 b was performed with the Las Cumbres Observatory Global Telescope (LCOGT; Brown et al. 2013) 0.4 m telescope at Haleakala on 2021 May 29. No eclipsing binaries were identified within $2''.5$ of the target.

Two observations were also collected with the 1.0 m LCOGT telescope of McDonald Observatory using the Sinistro instrument with the SDSS i' filter. The first of these covered a full transit of planet c on 2020 September 6 UT, and the second covered a partial transit of planet b on 2020 September 24 UT. These transits are used in the light curve model in Section 6.1. These data confirm that the transit events occur on-target relative to all known Gaia DR3 and TICv8 stars. The photometric aperture sizes used to extract the on-target detections were $7''.0$ for the 2020 September 6 observations and $4''.7$ for the 2020 September 4 observations.

On 2021 February 22 UT a partial transit of TOI-2095c was observed from the 1.6 m telescope at Observatoire du Mont-Mégantic (OMM). The photometric aperture radius was 10 pixels ($4''.66$). A partial transit is visible but the observations were ended prior to the completion of the transit due to high humidity. This partial transit was included in the transit timing variations analysis described in Section 6.3.

5. Vetting and Validation

Due to the shallow transits and long orbital periods of the two planets, the centroid and modshift measurements from the Discovery and Vetting of Exoplanets (DAVE) vetting pipeline (Kostov et al. 2019) are somewhat unreliable. This is demonstrated in Figure 4 showing the results for planet b for Sector 24. While the data are low signal-to-noise ratio (S/N) and only have two transits in this sector (shown in the upper right panel), there are no indications for a false positive.

A false-alarm detection due to random noise is highly unlikely, as both planets were detected in ground-based transits. However, a scenario where the signals detected are caused by background contaminating sources always exists. Having signals from two planets, as we have here, would require either two background eclipsing binaries or a background system of planets, both of which are unlikely scenarios. To demonstrate this we look at the statistical probability that the detections are false positives.

We statistically analyzed the likelihood of false-positive signals using the publicly available software package *vespa* (Morton 2012, 2015) to place a numerical value on the false-positive probability (FPP) of the signals. *vespa* combines the

³⁷ <https://tess.mit.edu/followup>

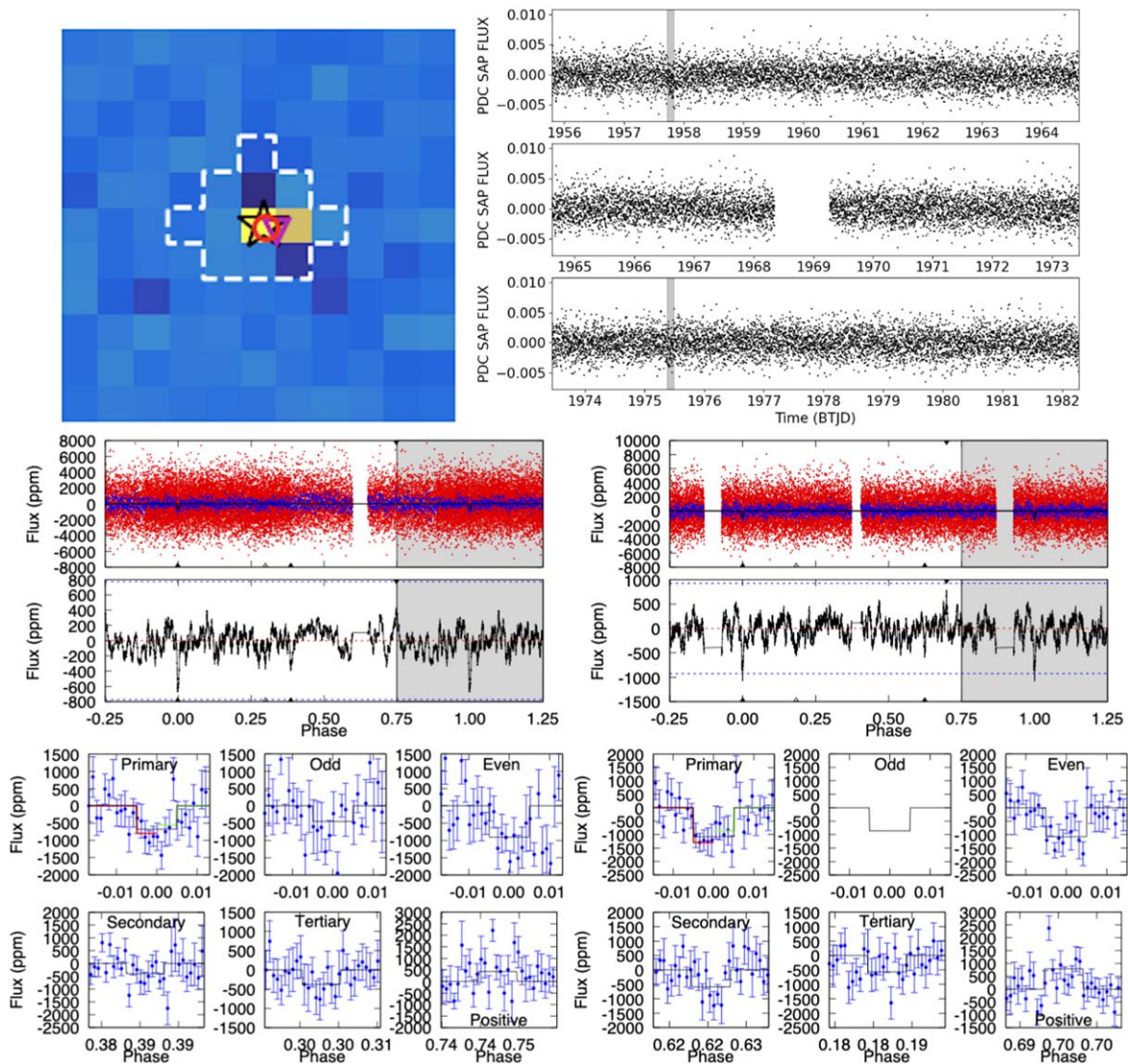


Figure 4. There are only two transits for TOI-2095.01 and only one for TOI-2095.02 in this sector, all with fairly low S/N, but there are no indications of false positives. Left: The difference image for TOI-2095 planet 1 for Sector 24, showing the position of the target (black star), the measured difference image photocenters from a point-spread-function and pixel-response-function (cyan triangle and red circle, respectively). Right: PDC SAP light curve of TOI-2095 for Sector 24 highlighting the two transits in the sector. Lower panels: Modshift results from DAVE, left for TOI-2095.01 and right for TOI-2095.02, respectively. The small panels show zoom-ins and corresponding fits to the primary transits, the odd and even transits, the most significant secondary transits, as well as to any additional negative (tertiary) or positive events.

host star properties, the observed TESS transits, and follow-up constraints to compare the signals to six astrophysical false-positive scenarios allowed by the remaining parameter space in a probabilistic framework: an unblended eclipsing binary (EB), a blended background EB, a hierarchical EB companion, and double period scenarios of these three. The output of *vespa* is the likelihood that a detected transit signal may be mimicked by one of these astrophysical false-positive scenarios. *vespa* assumes that the signal is coming from the target star, which was shown to be true for both signals in Section 4. The software was run on each transit signal individually after masking out transits from other planets. We included observational constraints in our analysis along with the addition of the Keck contrast curve (see Section 4). The final FPP values are 7.94×10^{-5} and 4.87×10^{-4} for TOI-2095 b and TOI-2095c, respectively. Both of these are $\ll 0.01$ and thus constitute firm validations of the planetary scenario.

As an independent check, we also ran these signals through another statistical validation software, TRICERATOPS (Giacalone et al. 2020). Developed specifically for use with TESS data, TRICERATOPS differs from *vespa* in that it accounts for the TESS extraction aperture and the actual background starfield when calculating the likelihood that the signal originates from a star nearby in the field of view. Otherwise, TRICERATOPS works similarly, testing the shape and depth of the transit against a suite of possible astrophysical false-positive scenarios to provide a final FPP as well as a Nearby FPP (NFFP) which is the probability that the signal is due to a false-positive scenario around a nearby star. We ran TRICERATOPS using the same inputs as VESPA with the addition of the apertures used to extract the PDC SAP light curves generated by the TESS SPOC. We find that TOI-2095 b has an FPP of $1.85 \pm 1.11 \times 10^{-3}$ and an NFFP of $1 \pm 1 \times 10^{-8}$ while TOI-2095c has an FPP of

$7.17 \pm 7.03 \times 10^{-2}$ and an NFPP of $<1 \times 10^{-8}$. As TOI-2095 b has an FPP > 0.015 and an NFPP $<10^{-3}$, this signal is considered validated. However, because the FPP for TOI-2095c is greater than the 0.015 threshold but is still less than 0.5 with an NFPP $<10^{-3}$, this signal is only a likely planet.

However, neither the FPPs from *vespa* nor those from TRICERATOPs account for the fact that this system is host to multiple signals, implying a lower FPP by $\sim 50\times$ due to what is termed a ‘‘multiplicity boost’’ (Lissauer et al. 2012; Guerrero et al. 2021). As this puts the FPP values for both planet candidates $\ll 1\%$, we consider these signals to be validated planets.

6. Data Analysis and Results

6.1. Light Curve Model

We modeled the transits of the two planets in the TOI-2095 system using a Bayesian framework to compute stellar and exoplanet parameters from a limb-darkened light curve model (Luger et al. 2019; Agol et al. 2020). We assumed a linear ephemeris and used initial parameters computed by the TESS pipeline (Jenkins et al. 2016), combined with the stellar properties calculated in Section 3.

Our transit model uses the TESS 2 minute cadence PDC SAP data (Smith et al. 2012; Stumpe et al. 2012, 2014), plus two observations from LCOGT. For a linear ephemeris, the addition of the available 20 s cadence data does not provide a significant improvement in the model fit. However, for the later analysis of transit timing variations (TTVs) in Section 6.3 we do include the higher-cadence data. We also do not include the partial transit of planet c from OMM here, although we again include it in the TTV section.

The parameters included in the model are: the stellar radius and density, two stellar limb-darkening parameters for each instrument (i.e., for TESS and LCOGT), the photometric zero-point (one for the entire TESS data set and one for each ground-based observation), and terms for additional white noise for each separate instrument configuration. In addition, for each planet we include a transit midpoint, orbital period, impact parameter, planet radius in units of the stellar radius, and two eccentricity vectors ($e \sin \omega$ and $e \cos \omega$). We use a Gaussian Process (GP) to model any variability in the time series that is not described by the model. The GP is a kernel stochastically driven, damped harmonic oscillator using the *celerite* package (Foreman-Mackey et al. 2017; Foreman-Mackey 2018), similar to the model described in (Gilbert et al. 2020). Separate hyperparameters are used for the GPs applied to TESS and LCOGT data.

The priors on the joint TESS and LCOGT model parameters are: Gaussian for the stellar radius, orbital period, mid-transit time, and photometric zero-point; log-normal for the stellar density and scaled planet radius; uniform between zero and one for the impact parameter; the limb-darkening parameters follow Kipping (2013). The prior means come from an initial fit to the data based on the transit search parameters, and the prior standard deviations were chosen to be only very weakly constraining so that the data are primarily responsible for constraining the posterior. The prior standard deviations were selected by performing a sensitivity analysis; setting the standard deviation at approximately 10 times the value at which the data constrains the posterior. The orbital periods and mid-transit times were 0.001 and 0.02 days, respectively, which

Table 4
Parameters Measured from the Light Curve Model

Parameter	Median	+1 σ	-1 σ
Star			
Stellar Radius	0.453	0.028	0.029
Stellar Density	6.7	1.2	1.1
TESS Limb-darkening u_1	0.23	0.25	0.17
TESS Limb-darkening u_2	0.12	0.33	0.23
LCOGT Limb-darkening u_1	0.927745	0.525472	0.572409
LCOGT Limb-darkening u_2	-0.19	0.52	0.42
TOI-2095 b			
Transit midpoint (BJD)	2459646.7038	0.0012	0.0012
Orbital Period (days)	17.664872	0.000045	0.000051
R_p/R_s	0.0263	0.0011	0.0011
Impact parameters	0.30	0.22	0.20
Eccentricity	0.12	0.19	0.08
Argument of periastron (degrees)	-17	140	130
Radius (R_\oplus)	1.30	0.10	0.10
a/R_s	48.0	2.7	2.7
Semimajor axis	0.1010	0.0088	0.0084
Inclination (degrees)	89.64	0.24	0.24
Transit Duration (hours)	2.72	0.37	0.43
Transit Depth ^a (R_p/R_s) ² (ppt)	0.693	0.061	0.062
Insolation Flux (S_\oplus)	3.23	0.64	0.54
TOI-2095 c			
Transit midpoint (BJD)	2459662.1464	0.0018	0.0020
Orbital Period (days)	28.17221	0.00011	0.00014
R_p/R_s	0.0282	0.0013	0.0013
Impact parameters	0.24	0.23	0.16
Eccentricity	0.13	0.18	0.09
Argument of periastron (degrees)	-55	100	92
Radius (R_\oplus)	1.39	0.11	0.10
a/R_s	65.6	3.7	3.6
Semimajor axis	0.138	0.012	0.011
Inclination (degrees)	89.79	0.14	0.18
Transit Duration (hours)	3.12	0.39	0.54
Transit Depth (R_p/R_s) ² (ppt)	0.796	0.071	0.069
Insolation Flux (S_\oplus)	1.73	0.34	0.28

Note.

^a The measured transit depth, accounting for limb darkening, for the two planets was 0.776 and 0.901 ppt.

are a factor of 10 larger than the posterior standard deviations. The reason for using a Gaussian rather than a Uniform distribution is one of practicality. The sampling is more stable when the priors are not improper. We include two components in a prior on eccentricity: we have a 1/eccentricity prior owing to the bias of sampling in vector space, and we include a Beta prior following Kipping (2013) with hyperparameters from Van Eylen et al. (2019) using the values for multiplanet systems.

We built this model in the *exoplanet* software (Foreman-Mackey et al. 2021) which is built on *PyMC* (Salvatier et al. 2016), a Python library that allows users to build Bayesian models and sample them using Markov Chain Monte Carlo methods. We use the No U-turn Sampler (NUTS; Hoffman & Gelman 2014) which is a form of Hamiltonian Monte Carlo. We used 3000 samples to tune the posterior and 3000 to sample the posterior distribution. We did this for four independent chains so that we could use these to test for convergence. All chains had consistent results, so we combined the chains into a single set of posterior samples.

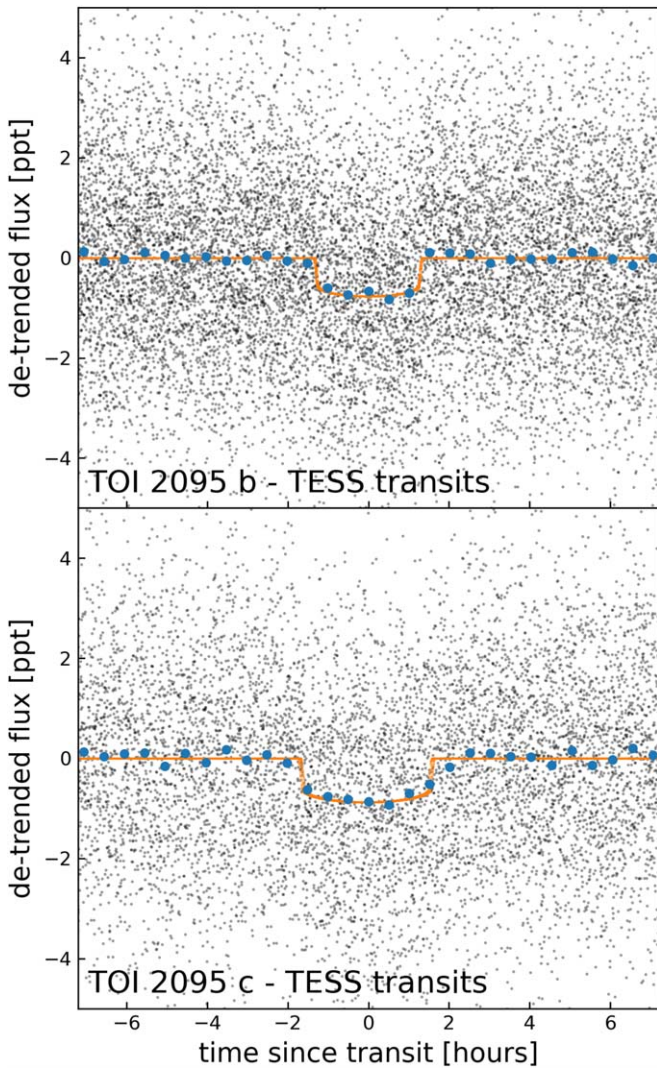


Figure 5. Folded TOI-2095 b and c transits observed by TESS. The gray points are the observed data, folded on the best-fitting orbital period, the blue dots are binned data, and the orange curve is the best-fitting transit model.

The results of this sampling are provided in Table 4. The two planets have radii of 1.30 ± 0.10 and $1.39 \pm 0.11 R_{\oplus}$. Folded transits from the TESS data are shown in Figure 5, and the two LCOGT epochs of data are shown in Figure 6. The orbital eccentricities of both planets are consistent with zero. We used the samples to compute additional planet parameters, that are also listed in the table: the orbital inclination, semimajor axis, insolation flux, and transit duration. The two planets have insulations of 3.2 and 1.7 times the Earth’s insolation from the Sun.

We also ran independent fits of the TOI-2095 system using the Cycle 2 light curve from TESS with EXOFASTv2 (Eastman et al. 2019) and found the fitted parameters to be consistent within 1σ of the results presented here.

We also ran a separate model to verify that the stellar properties recovered from the light curve data were consistent with the stellar modeling work in Section 3. We used the same model except we used a Uniform prior on stellar density rather than a Gaussian prior taken from the stellar modeling. Our analysis recovered a density of $5.5 \pm 3.0 \text{ g cm}^{-3}$, which is

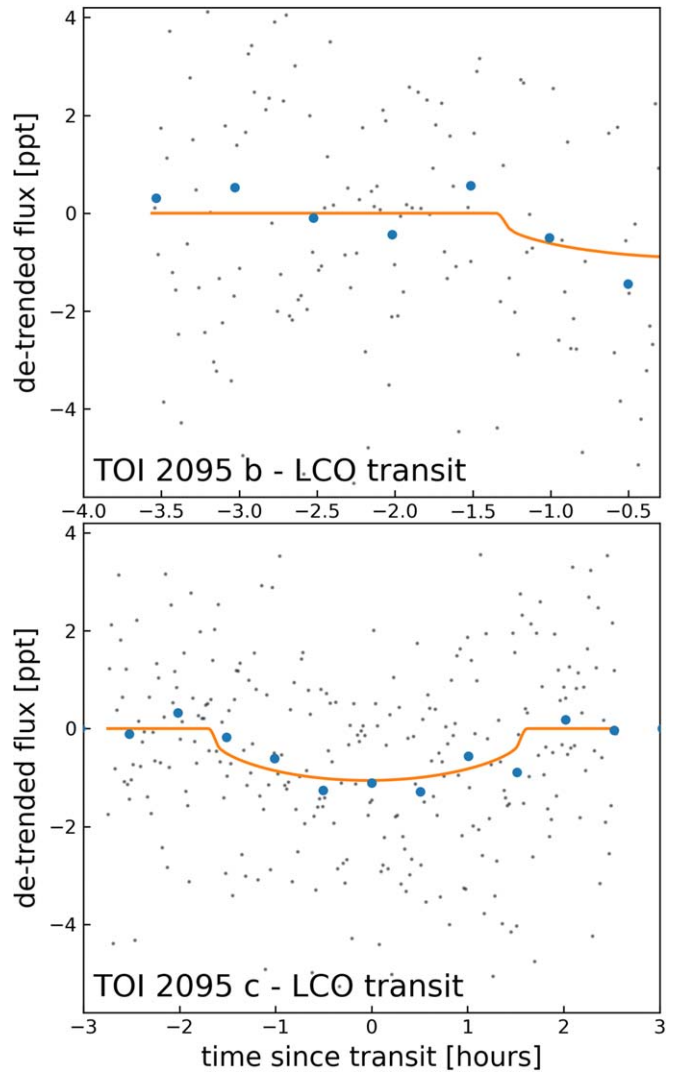


Figure 6. Two transits of TOI-2095 observed by LCOGT. The upper panel shows the partial transit of planet b and the lower panel shows the full transit of planet c.

consistent with the value of $7.4 \pm 1.4 \text{ g cm}^{-3}$ from section Section 3.

6.2. System Dynamics

We performed $\sim 10^4$, 1 Myr simulations investigating the long-term dynamical stability of the TOI-2095 system. Our simulations are based on the Mercury6 hybrid integration package (Chambers 1999), and span a range of plausible densities and eccentricities for each planet ($\sim 1\text{--}12 \text{ g cm}^{-2}$ and 0.0–0.5, respectively). This allows us to account for the substantial degeneracy in planet masses (e.g., Chen & Kipping 2017). Unique initial conditions for each simulation are created by utilizing each planet’s nominal semimajor axis and inclination and assigning the remaining angular orbital elements randomly by sampling uniform distributions of angles.

In general, we find the TOI-2095 system to be dynamically stable when the planets originate on noncrossing orbits ($e \lesssim 0.3$ for each planet) for the range of masses we test. This is not surprising given the well-spaced nature of the system in terms of mutual-Hill radii (Chambers et al. 1996). It is important to

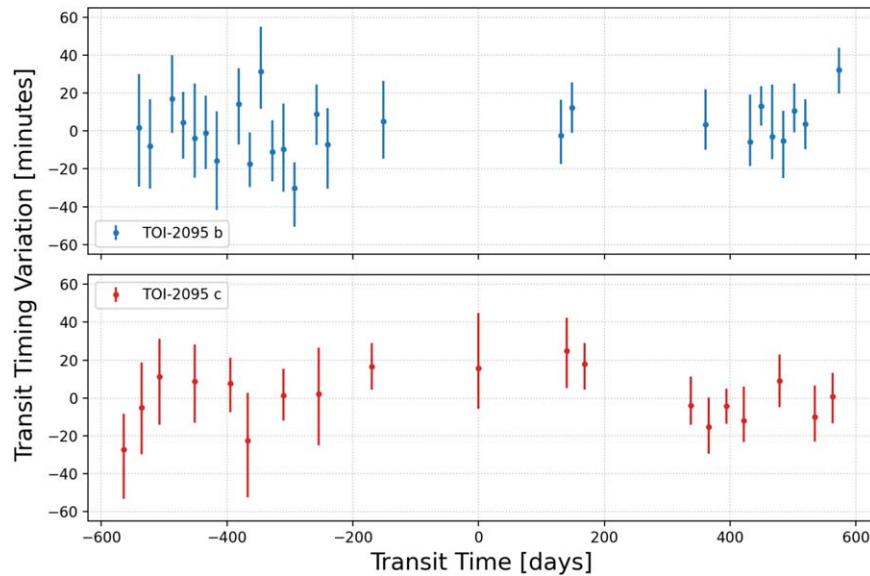


Figure 7. Observed minus calculated transit times for TOI-2095 b and c show no significant evidence for TTVs at this time. However, the number of transits is limited, and further observations may reveal a longer superperiod for transit times.

note that the length of our simulations ($\sim 10^7$ orbits for the inner planet) is likely insufficient to fully characterize the system’s dynamical state and make a comprehensive determination of its stability (e.g., Lithwick & Wu 2011). Moreover, we do not consider the possibility of perturbations from other planets in these simulations. Thus, while our simulations do not prove that TOI-2095 is stable, they strongly suggest that it is stable on long timescales.

6.3. Modeling Transit Timing Variations

In addition to the transit modeling with the planets orbiting on linear ephemerides presented in Section 6.1, we also generated a model that allowed the transit times to vary. This model enabled us to search for transit timing variations caused by either the two planets perturbing each other, or from a third body in the system. The model was very similar to the linear ephemeris model, except that (i) we used 20 s cadence data where available, (ii) we added a partial transit observed by the 1.6 m telescope at Observatoire du Mont-Mégantic of TOI-2095c (iii) we enabled the transit times to shift from the linear ephemeris, with a Gaussian prior with a standard deviation of 0.03 days and a mean of zero relative to linear ephemeris, and (iv) we only allowed circular orbits. The reason for only allowing circular orbits here is that we are only interested in measuring the transit times, and neglecting noncircular orbits speeds up the calculation.

We did not detect significant transit timing variations for either planet over the 1170 day span that the observations cover. Figure 7 shows the deviation from a linear ephemeris for the two planets. Planet b shows flat light TTV curves. However, the TTV model for TOI-2095c shows hints of a turnover in the transit times (the first and last transits are earlier and the central transits occur later). This may be something to investigate further with additional TESS transit observations.

7. Discussion

7.1. Implications for Planet Formation

A large fraction of the known super-Earth and sub-Neptune populations reside in multiple-planet systems that display a remarkable degree of intra-system uniformity (Adams 2019; Weiss et al. 2022), in terms of planet masses, sizes, and circular/coplanar orbits. While there exists ongoing debate about the theories that support the so-called peas-in-a-pod phenomena for the population of compact multiplanet systems, the architecture of the TOI-2095 planetary system is consistent with these patterns. The TOI-2095 planet sizes are comparable, the period ratio of the TOI-2095 planets resides in the middle of the distribution of peas-in-a-pod systems, and the outer planet is slightly larger. Assuming this theory holds, we would expect the next outer planet (if one were to exist) to reside within a near 45 day period, which could motivate future transit searches if more data and a longer baseline are collected (which is feasible given TESS has been successful with extended missions).

The TOI-2095 system also provides an excellent laboratory to test the formation mechanisms of the super-Earth and mini-Neptune populations. For close-in planets, photoevaporation and core-powered mass loss have been proposed as mechanisms that induce atmosphere loss and may explain this bimodality (e.g., Owen & Wu 2013; Owen 2017; Ginzburg et al. 2018; Gupta & Schlichting 2019; Cloutier & Menou 2020; Gupta & Schlichting 2020). However, small planets on wider orbits (greater than about 20 days around M dwarfs), such as TOI-2095 b (17.7 days) and TOI-2095c (28.2 days), present an opportunity to distinguish between formation pathways (Lee et al. 2022). This is because, at wide separations, the atmospheric mass loss timescales for small rocky planets often exceed the age of the planetary system. As a result, long-period rocky planets must have formed rocky and therefore are not being sculpted by atmospheric escape. This motivates follow-up mass measurements of the TOI-2095 planets to determine if

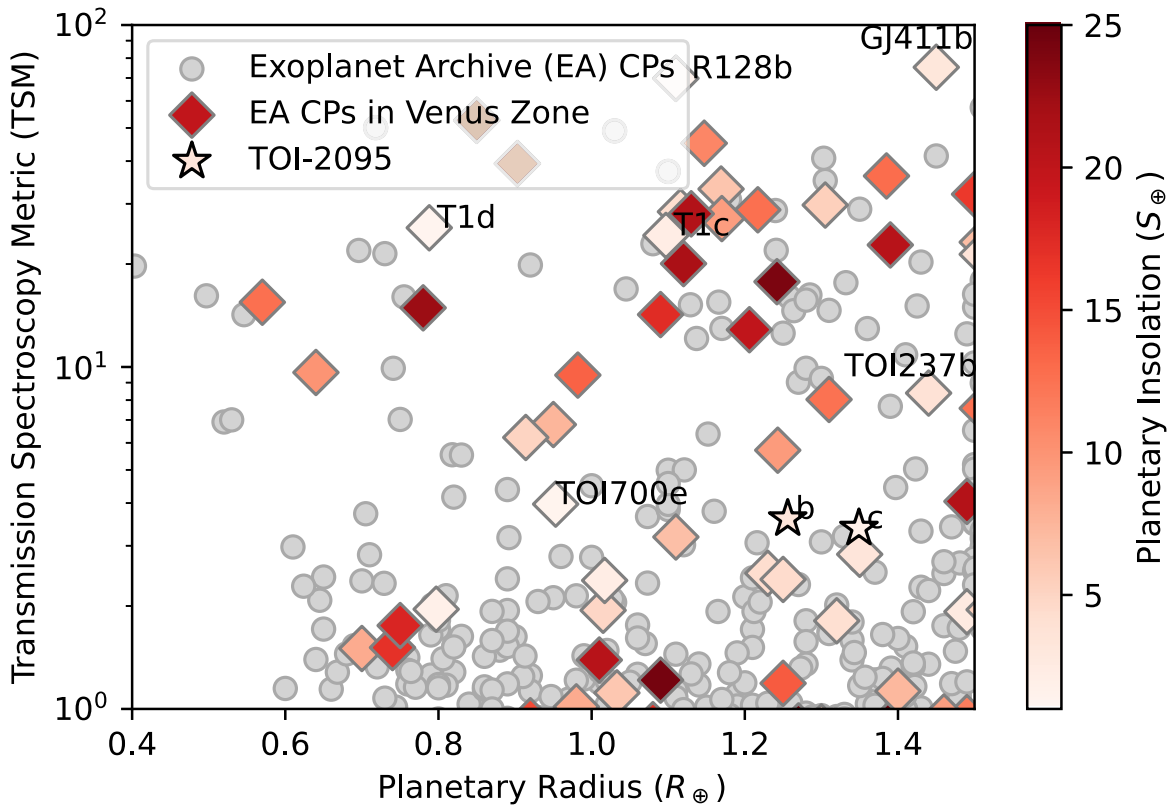


Figure 8. Transmission Spectroscopy Metric (TSM) for the TOI-2095 planets, compared to the TSM for confirmed planets (CP) in the NASA Exoplanet Archive. The color bar indicates other planets within the VZ. We label those planets near the outer edge of the VZ with equilibrium temperatures less than 400 K. Table 5 lists the properties of the eight planets labeled in this figure.

they are rocky and to (potentially) rule out proposed formation mechanisms that rely on atmospheric escape.

7.2. Constraints on Stellar Activity

Stellar variability has long been a challenge to interpreting the nature of transiting planets orbiting low-mass stars. This is true both for measuring the mass of planets (Suárez Mascareño et al. 2015) and also for detecting atmospheric features (Rackham et al. 2018; Barclay et al. 2021; Moran et al. 2023). We examined the level of stellar activity present in the data sets we have collected, focusing on the TRES spectroscopic observations and the TESS photometric time series. From the TRES spectrum we found an equivalent width of $H\alpha$, following Newton et al. (2017) and West et al. (2011), of $EW_{H\alpha} = 0.277 \pm 0.012 \text{ \AA}$. This places TOI-2095 firmly on the quiet edge of the quiescent M-dwarf sample (Newton et al. 2017). The resolving power of TRES is not high enough to detect the rotational broadening but an appropriate upper limit based on the nondetection is $v \sin i < 2 \text{ km s}^{-1}$. If the stellar rotation and planetary orbits are aligned, this would indicate that the star is not rapidly rotating (rotation period longer than 11 days), consistent with the findings from the $EW_{H\alpha}$ analysis.

The TESS light curve similarly shows no evidence of activity on the star. There are no flares present, and no obvious rotational modulation above the noise level of the star. The 1-hr combined differential photometric precision (CDPP) varies between 350 and 550 ppm over the different TESS sectors and is consistently below the median variability for all stars at this brightness and within the envelope of quiet stars. This indicates

that this star does exhibit short-timescale variability above the TESS noise level.

7.3. Prospects for Atmospheric Characterization

To determine the suitability of the TOI-2095 planets for atmospheric characterization, we computed the Transmission Spectroscopy Metric (TSM) and Emission Spectroscopy Metric (ESM; Kempton et al. 2018), standardized metrics which are proportional to the expected transmission or emission S/N for a relevant JWST observation, for the planets. We then compared those values to the TSM and ESM of all confirmed planets listed within the NASA Exoplanet Archive.³⁸ Figure 8 shows this comparison, with Venus zone (VZ) planets depicted in color according to their insolation flux, and all other planets in gray. We followed the methodology of Kane et al. (2014) and Ostberg & Kane (2019) to define the boundaries of the VZ. In particular, the inner edge of the VZ is set to $25S_{\oplus}$, coinciding with the amount of flux that would place Venus on the Cosmic Shoreline, where the planet would start to experience severe atmospheric loss (Zahnle & Catling 2017). We adopted the Runaway Greenhouse boundary as the outer edge of the VZ. The effective insolation flux at this boundary depends on the stellar type and is defined by Kopparapu et al. (2013, 2014) as

$$S_{\text{eff}} = S_{\text{eff},\odot} + aT_{\star} + bT_{\star}^2 + cT_{\star}^3 + dT_{\star}^4, \quad (1)$$

where $T_{\star} = T_{\text{eff}} - 5780 \text{ K}$. Kopparapu et al. (2013) provide the coefficients for stellar temperatures $2600 \text{ K} \leq T_{\text{eff}} \leq 7200 \text{ K}$ as

³⁸ NASA Exoplanet Archive, <https://exoplanetarchive.ipac.caltech.edu/>, accessed on 1 November 2022.

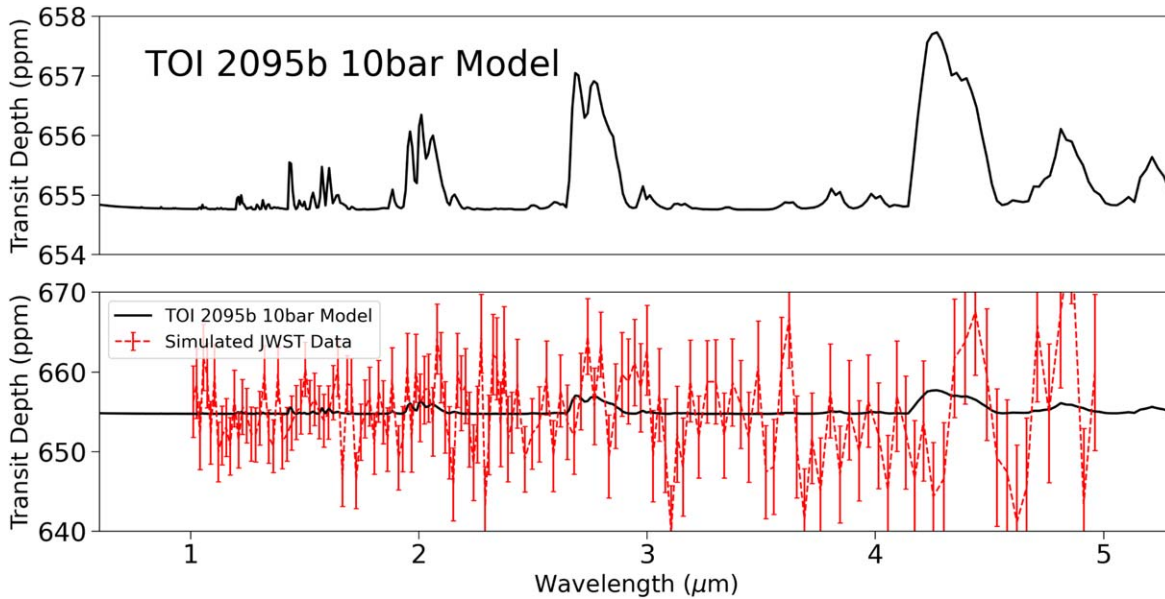


Figure 9. An estimated transmission spectrum of TOI-2095 b with a 10 bar, cloudless Venus-like atmosphere (upper plot), and simulated JWST data of the same planet assuming 100 transit observations (lower plot). Note that the black line is the same spectrum in both the upper and lower plots, but the scale of the y-axis is larger in the lower plot to capture the uncertainty in the simulated JWST data.

Table 5
Comparison of TOI-2095 to other VZ Planets with $T_{\text{eq}} < 400$ K

Planet Name	TSM	R_p (R_{\oplus})	M_p (M_{\oplus})	R_* (R_{\odot})	T_{eq} (K)	m_J (mag)	S_p (S_{\oplus})
TRAPPIST-1 d	25.688	0.788	0.388	0.120	288.	11.354	1.11
TRAPPIST-1 c	24.406	1.097	1.308	0.120	342.	11.354	2.21
TOI-237 b	8.389	1.440	2.670 [†]	0.210	388.	11.740	3.70
TOI-700 e	3.972	0.953	0.818 [†]	0.420	273.	9.469	1.27
TOI-2095 b	3.598	1.256	2.116 [†]	0.451	375.	9.797	3.26
TOI-2095c	3.377	1.349	2.389 [†]	0.451	320.	9.797	1.75

Note.

[†]Masses Estimated given the Planet Radii.

$S_{\text{eff},\odot} = 1.0512$, $a = 1.3242 \times 10^{-4}$, $b = 1.5418 \times 10^{-8}$, $c = -7.9895 \times 10^{-12}$, and $d = -1.8328 \times 10^{-15}$.

In order to estimate TSM values for TOI-2095 b and c, we estimated masses for the planets using the formula $1.436R_p^{1.7}$ (Kempton et al. 2018; Louie et al. 2018), which is based upon the Chen & Kipping (2017) mass–radius relationship. Following Kempton et al. (2018), we calculated planetary equilibrium temperature assuming zero albedo and uniform day–night heat redistribution. Using these values, we computed TSM to be 3.60 and 3.38 and ESM to be 0.29 and 0.15 for TOI-2095 b and TOI-2095c, respectively. All other quantities required to calculate TSM and ESM for the TOI-2095 planets are taken from Tables 3 and 4 of this work. In actuality, nonzero albedo and nonuniform heat redistribution can significantly impact the potential atmospheric composition and detectability and these assumptions should be carefully considered prior to any potential spectroscopic investigation. However, the TSM and ESM remain valuable tools for comparing the potential observability of spectroscopic features between observation candidates in the absence of more in-depth knowledge.

In Table 5, we compare the TSM values between the TOI-2095 planets and other VZ planets that have equilibrium temperatures less than 400 K (TRAPPIST-1 d, TRAPPIST-1 c, TOI-237 b, and TOI-700 e; Gillon et al. (2016), Waalkes et al. (2021),

Gilbert et al. (2023)). Although six confirmed VZ planets with $R_p < 1.5R_{\oplus}$ have higher TSM values, the TOI-2095 planets offer observational advantages. Namely, the planets are within the TESS and JWST CVZs, making it easier to schedule multiple transit observations. The host star is relatively bright, yet not so bright that saturation may be an issue with most JWST near-infrared instruments.³⁹

7.4. Venus Analogs

Recent studies of planetary habitability have emphasized the need to leverage the limited data inventory of terrestrial atmospheres from within the solar system (i.e., of Earth, Venus, and Mars; Kane et al. 2021b). In particular, understanding the atmospheric and interior evolution of Venus is considered critical within the context of planetary habitability and as a parallel to an Earth-based climate model (Popp et al. 2016; Kane et al. 2019; Margot et al. 2021; Kane 2022). Models of early Venus suggest that water may never have condensed on the surface due to an extended magma phase (Hamano et al. 2013) and/or cloud formation on the night side on the planet (Turbet et al. 2021). Alternatively, for scenarios in which surface water condensation

³⁹ NIRSpec Prism mode generally saturates at $m_J \lesssim 10.5$, so only this instrument mode may present problems for the TOI-2095 system.

occurred, Venus may have maintained temperate surface conditions for several billion years, enabled by cloud formation at the substellar point (Way et al. 2016; Way & Del Genio 2020). In fact, it has been shown that both a habitable and waterless past for Venus self-consistently reproduce modern bulk atmospheric composition, inferred surface heat flow, and observed ^{40}Ar and ^4He (Krissansen-Totton et al. 2021), further underscoring the need for additional investigations. In addition, early orbital dynamic effects may have enhanced water loss from the young Venus (Kane et al. 2020), an effect that may have a more pronounced influence for eccentric exoplanets (Barnes et al. 2013; Palubski et al. 2020). Venus also serves as a local laboratory for atmospheric loss effects, with application to exoplanets (Dong et al. 2020). A detailed investigation of these various facets of our sister planet required significantly more planetary data, which has motivated further Venus missions over the coming decade (Ghail et al. 2020; Garvin et al. 2022; Smrekar et al. 2022).

Numerous discovered exoplanets have been proposed as potential exoVenus candidates, including Kepler-69 c (Kane et al. 2013), Kepler-1649 b (Angelo et al. 2017; Kane et al. 2018, 2021a), TRAPPIST-1 c (Lincowski et al. 2018), and GJ 3929 b (Beard et al. 2022). Indeed, the large number of close-in exoplanets has enabled a statistical consideration of Venus Zone planet occurrence rates (Kane et al. 2014), along with suitable targets for atmospheric follow-up observations (Lustig-Yaeger et al. 2019a; Lincowski et al. 2019; Ostberg & Kane 2019; Ostberg et al. 2023). Such follow-up work requires a detailed knowledge of the Venusian atmospheric chemistry and structure, and how these details manifest in the expected spectral signatures that are acquired (Schaefer & Fegley 2011; Ehrenreich et al. 2012; Barstow et al. 2016; Jordan et al. 2021). As described in Section 7.3 and shown in Figure 8, the TOI-2095 planets fall alongside numerous other interesting exoVenus candidates and present additional prospects for studying terrestrial atmospheric evolution as a function of such aspects as planetary radius and insolation flux.

Currently, the primary method for studying the atmospheric composition of Venus-like worlds is through transmission spectroscopy, which is used to determine the wavelengths at which light is absorbed when passing through a planet's atmosphere. Venus' transmission spectrum was modeled in preparation for the transit of Venus in 2012, which demonstrated that the Venusian cloud and haze layers prevent transmission spectroscopy from probing the atmosphere below an altitude of 80 km (Ehrenreich et al. 2012). Lincowski et al. (2018) modeled the transmission spectra of the TRAPPIST-1 planets assuming they had 10-bar as well as 92.1 bar (the surface pressure of Venus) Venus-like atmospheres. In both cases, their work illustrated that the weaker CO_2 absorption bands at 1.05 and 1.3 μm and absorption caused by sulfuric acid clouds are likely to be the best avenues for determining if a planet has a Venus-like atmosphere and may help constrain a high CO_2 abundance. Simulated JWST observations of the TRAPPIST-1 planets with Venus-like atmospheres showed that their atmospheres could be detected in less than 20 transit observations, but discerning their compositions would take more than 60 transit observations (Lustig-Yaeger et al. 2019b). We adopted a similar approach and estimated the transmission spectrum of TOI-2095 b with a cloudless, 10 bar Venus-like atmosphere using the Planetary Spectrum Generator (PSG; Villanueva et al. 2018). We simulated 100 JWST transit observations of this hypothetical TOI-2095 b Venus, and while CO_2 absorption features could be seen at 2.0, 2.7, and 4.3 μm ,

these features were only a few ppm in depth, which is far too small to be detected by JWST. Better constraints on the viability of atmospheric studies with the TOI-2095 system can be provided if mass measurements are obtained.

8. Summary and Conclusions

The TOI-2095 two-planet system provides another valuable system discovered by TESS that is amenable to follow-up observations that can place constraints on the system's bulk composition and formation history. The star, a 0.47 solar mass M1V dwarf, lies in the TESS continuous viewing zone, and we present results based on 24 TESS sectors.

This multiplanet system is dynamically stable, and no signs of transit timing variations have been observed thus far (although a longer baseline of additional TESS observations could reveal TTVs). Among the most exciting prospects for characterizing the TOI-2095 system is the potential for obtaining precise radial velocity mass measurements. With relatively wide orbits, establishing the composition and determining whether either planet is indeed rocky will provide valuable clues into the formation mechanisms that sculpt the widely studied, but still widely debated, problem of why a radius valley exists between rocky planets and those with H/He envelopes.

The TOI-2095 planets are only about 30% larger than the Earth, and have insolation values between 1.7 and 3.2 times that which Earth receives from the Sun, placing them in the Venus-class regime. We explored the feasibility of transmission and emission spectroscopic measurements to probe their atmospheres via missions like JWST. While the calculated metrics (TSM and ESM) that indicate their potential for such measurements rank lower than six other small exoplanets in the Venus-class regime, TOI-2095 is a relatively quiet star which is beneficial for interpreting atmospheric spectra. We simulated the transmission spectrum of TOI-2095 b assuming a cloudless, 10 bar Venus-like atmosphere, and found that CO_2 absorption features would be far too small to be detected by JWST. As we obtain more data on the atmospheres and compositions of Venus zone planets (such as the JWST observations of the TRAPPIST-1 planets), we will gain a better understanding of the assumptions and range of inputs that can better simulate and model this class of planets, as well as the key observables we should look for in high-precision JWST data that can place these small planets into context.

The field of transiting exoplanet science is bright, and missions like TESS, and upcoming missions Nancy Grace Roman Space Telescope and PLATO, have the potential to deliver many thousands of additional exoplanets to study (Montet et al. 2017; Barclay et al. 2018). Systems that orbit bright stars and are amenable to follow-up studies, like TOI-2095, offer an excellent opportunity to shed light on composition and formation theories and ultimately identify trends that will set the stage for the interpretation of exoplanet populations revealed by future missions.

Acknowledgments

We are thankful for support from GSFC Sellers Exoplanet Environments Collaboration (SEEC), which is funded by the NASA Planetary Science Division's Internal Scientist Funding Model. The material is based upon work supported by NASA under award number 80GSFC21M0002. Additionally, a portion of this work was supported by NASA's Astrophysics

Data Analysis Program through grant 20-ADAP20-0016. This research was carried out in part at the Jet Propulsion Laboratory, California Institute of Technology, under a contract with the National Aeronautics and Space Administration (80NM0018D0004). B.J.H. acknowledges support from the Future Investigators in NASA Earth and Space Science and Technology (FINESST) program grant 80NSSC20K1551. T.A. B.'s and D.R.L.'s research activities were supported by an appointment to the NASA Postdoctoral Program at the NASA Goddard Space Flight Center, administered by Oak Ridge Associated Universities under contract with NASA. K.A.C. acknowledges support from the TESS mission via subaward s3449 from MIT.

This paper includes data collected by the TESS mission, which are publicly available from the Mikulski Archive for Space Telescopes (MAST). Funding for the TESS mission is provided by NASA's Science Mission Directorate. We acknowledge the use of public TESS Alert data from pipelines at the TESS Science Office and at the TESS Science Processing Operations Center. Resources supporting this work were provided by the NASA High-End Computing (HEC) Program through the NASA Advanced Supercomputing (NAS) Division at Ames Research Center for the production of the SPOC data products. This research has made use of the Exoplanet Follow-up Observation Program website, which is operated by the California Institute of Technology, under contract with the National Aeronautics and Space Administration under the Exoplanet Exploration Program. This work has made use of data from the European Space Agency (ESA) mission Gaia (<https://www.cosmos.esa.int/gaia>), processed by the Gaia Data Processing and Analysis Consortium (DPAC; <https://www.cosmos.esa.int/web/gaia/dpac/consortium>). Data presented herein were obtained at the W. M. Keck Observatory, which is operated as a scientific partnership among the California Institute of Technology, the University of California, and the National Aeronautics and Space Administration. The Observatory was made possible by the generous financial support of the W. M. Keck Foundation. The authors acknowledge the USNA Advanced Research Computing Support (ARCS) office (<https://www.usna.edu/ARCS/>) which was made available for conducting the research reported in this paper. The material is based upon work supported by NASA under award No. 80GSFC21M0002. This work makes use of observations from the LCOGT network. Part of the LCOGT telescope time was granted by NOIRLab through the Mid-Scale Innovations Program (MSIP). MSIP is funded by NSF.




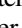





































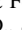
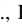


This research has made use of the NASA Exoplanet Archive, which is operated by the California Institute of Technology, under contract with the National Aeronautics and Space Administration under the Exoplanet Exploration Program. This research has made use of the Exoplanet Follow-up Observation Program (ExoFOP; DOI: 10.26134/ExoFOP5) website, which is operated by the California Institute of Technology, under contract with the National Aeronautics and Space Administration under the Exoplanet Exploration Program.

Facilities: TESS, LCOGT (Sinistro), OMM:1.6, Keck:II (NIRC2), FLWO:1.5m (TRES), Exoplanet Archive, ExoFOP, Gaia

Software: Arviz (Kumar et al. 2019), AstroImageJ (Collins et al. 2017), astropy (Astropy Collaboration et al. 2013, 2018), celerite2 (Foreman-Mackey et al. 2017; Foreman-Mackey 2018), exoplanet (Foreman-Mackey et al. 2021), DAVE

(Kostov et al. 2019), IPython (Perez & Granger 2007), Jupyter (Kluyver et al. 2016), Lightkurve (Lightkurve Collaboration et al. 2012), Matplotlib (Hunter 2007), Mercury6 (Chambers 1999), NumPy (van der Walt et al. 2011), Pandas (McKinney et al. 2010), PyMC3 (Salvatier et al. 2016), STARRY (Luger et al. 2019; Agol et al. 2020), Tapir (Jensen 2013), Theano (Theano Development Team 2016), TRICERATOPS (Giacalone et al. 2020), vespa (Morton 2012, 2015)

ORCID iDs

Elisa V. Quintana  <https://orcid.org/0000-0003-1309-2904>
 Emily A. Gilbert  <https://orcid.org/0000-0002-0388-8004>
 Thomas Barclay  <https://orcid.org/0000-0001-7139-2724>
 Michele L. Silverstein  <https://orcid.org/0000-0003-2565-7909>
 Joshua E. Schlieder  <https://orcid.org/0000-0001-5347-7062>
 Ryan Cloutier  <https://orcid.org/0000-0001-5383-9393>
 Samuel N. Quinn  <https://orcid.org/0000-0002-8964-8377>
 Joseph E. Rodriguez  <https://orcid.org/0000-0001-8812-0565>
 Andrew Vanderburg  <https://orcid.org/0000-0001-7246-5438>
 Benjamin J. Hord  <https://orcid.org/0000-0003-3904-6754>
 Dana R. Louie  <https://orcid.org/0000-0002-2457-272X>
 Stephen R. Kane  <https://orcid.org/0000-0002-7084-0529>
 Kelsey Hoffman  <https://orcid.org/0000-0001-6541-0754>
 Jason F. Rowe  <https://orcid.org/0000-0002-5904-1865>
 Giada N. Arney  <https://orcid.org/0000-0001-6285-267X>
 Matthew S. Clement  <https://orcid.org/0000-0001-8933-6878>
 Fred C. Adams  <https://orcid.org/0000-0002-8167-1767>
 Travis Berger  <https://orcid.org/0000-0002-2580-3614>
 Allyson Bieryla  <https://orcid.org/0000-0001-6637-5401>
 Paul Bonney  <https://orcid.org/0000-0002-4473-0297>
 Patricia Boyd  <https://orcid.org/0000-0003-0442-4284>
 Charles Cadieux  <https://orcid.org/0000-0001-9291-5555>
 Douglas Caldwell  <https://orcid.org/0000-0003-1963-9616>
 David R. Ciardi  <https://orcid.org/0000-0002-5741-3047>
 David Charbonneau  <https://orcid.org/0000-0002-9003-484X>
 Karen A. Collins  <https://orcid.org/0000-0001-6588-9574>
 Knicole D. Colón  <https://orcid.org/0000-0001-8020-7121>
 Dennis M. Conti  <https://orcid.org/0000-0003-2239-0567>
 Jessie Dotson  <https://orcid.org/0000-0003-4206-5649>
 Thomas Fauchez  <https://orcid.org/0000-0002-5967-9631>
 Erica J. Gonzales  <https://orcid.org/0000-0002-9329-2190>
 Maximilian N. Günther  <https://orcid.org/0000-0002-3164-9086>
 Christina Hedges  <https://orcid.org/0000-0002-3385-8391>
 Giovanni Isopi  <https://orcid.org/0000-0002-8458-0588>
 Ravi Kopparapu  <https://orcid.org/0000-0002-5893-2471>
 Avi Mandell  <https://orcid.org/0000-0002-8119-3355>
 Susan E. Mullally  <https://orcid.org/0000-0001-7106-4683>
 Rishi R. Paudel  <https://orcid.org/0000-0002-8090-3570>
 Brian P. Powell  <https://orcid.org/0000-0003-0501-2636>
 George R. Ricker  <https://orcid.org/0000-0003-2058-6662>
 Boris S. Safonov  <https://orcid.org/0000-0003-1713-3208>
 Richard P. Schwarz  <https://orcid.org/0000-0001-8227-1020>
 Keivan G. Stassun  <https://orcid.org/0000-0002-3481-9052>
 Joshua N. Winn  <https://orcid.org/0000-0002-4265-047X>
 Roland K. Vanderspek  <https://orcid.org/0000-0001-6763-6562>

References

- Adams, F. C. 2019, *MNRAS*, 488, 1446
 Agol, E., Luger, R., & Foreman-Mackey, D. 2020, *AJ*, 159, 123
 Allard, F., Homeier, D., & Freytag, B. 2012, *RSPITA*, 370, 2765
 Angelo, I., Rowe, J. F., Howell, S. B., et al. 2017, *AJ*, 153, 162

- Astropy Collaboration, Price-Whelan, A. M., Sipőcz, B. M., et al. 2018, *AJ*, **156**, 123
- Astropy Collaboration, Robitaille, T. P., Tollerud, E. J., et al. 2013, *A&A*, **558**, A33
- Barclay, T., Burke, C. J., Howell, S. B., et al. 2013, *ApJ*, **768**, 101
- Barclay, T., Kostov, V. B., Colón, K. D., et al. 2021, *AJ*, **162**, 300
- Barclay, T., Pepper, J., & Quintana, E. V. 2018, *ApJS*, **239**, 2
- Barnes, R., Mullins, K., Goldblatt, C., et al. 2013, *AsBio*, **13**, 225
- Barstow, J. K., Aigrain, S., Irwin, P. G. J., Kendrew, S., & Fletcher, L. N. 2016, *MNRAS*, **458**, 2657
- Beard, C., Robertson, P., Kanodia, S., et al. 2022, *ApJ*, **936**, 55
- Benedict, G. F., Henry, T. J., Franz, O. G., et al. 2016, *AJ*, **152**, 141
- Borucki, W. J., Koch, D., Basri, G., et al. 2010, *Sci*, **327**, 977
- Brown, T. M., Baliber, N., Bianco, F. B., et al. 2013, *PASP*, **125**, 1031
- Chambers, J. E. 1999, *MNRAS*, **304**, 793
- Chambers, J. E., Wetherill, G. W., & Boss, A. P. 1996, *Icar*, **119**, 261
- Chen, J., & Kipping, D. 2017, *ApJ*, **834**, 17
- Cloutier, R., & Menou, K. 2020, *AJ*, **159**, 211
- Collins, K. 2019, AAS Meeting Abstracts, **233**, 140.05
- Collins, K. A., Kielkopf, J. F., Stassun, K. G., & Hessman, F. V. 2017, *AJ*, **153**, 77
- Cutri, R. M., Skrutskie, M. F., van Dyk, S., et al. 2003, The IRSA 2MASS All-Sky Point Source Catalog (Washington, DC: NASA)
- Cutri, R. M., Wright, E. L., Conrow, T., et al. 2021, *yCat*, **II/328**
- Dieterich, S. B., Henry, T. J., Jao, W.-C., et al. 2014, *AJ*, **147**, 94
- Dong, C., Jin, M., & Lingam, M. 2020, *ApJL*, **896**, L24
- Eastman, J. D., Rodriguez, J. E., Agol, E., et al. 2019, arXiv:1907.09480
- Ehrenreich, D., Vidal-Madjar, A., Widemann, T., et al. 2012, *A&A*, **537**, L2
- Foreman-Mackey, D. 2018, *RNAAS*, **2**, 31
- Foreman-Mackey, D., Agol, E., Ambikasaran, S., & Angus, R. 2017, *AJ*, **154**, 220
- Foreman-Mackey, D., Luger, R., Agol, E., et al. 2021, *JOSS*, **6**, 3285
- Fulton, B. J., Petigura, E. A., Howard, A. W., et al. 2017, *AJ*, **154**, 109
- Gaia Collaboration, Prusti, T., de Bruijne, J. H. J., et al. 2016, *A&A*, **595**, A1
- Gaia Collaboration, Vallenari, A., Brown, A. G. A., et al. 2023, *A&A*, **674**, A1
- Garvin, J. B., Getty, S. A., Arney, G. N., et al. 2022, *PSJ*, **3**, 117
- Ghail, R., Wilson, C., Widemann, T., et al. 2020, *EPSC*, **2020**, EPSC2020
- Giacalone, S., Dressing, C. D., Jensen, E. L., et al. 2020, *AJ*, **161**, 24
- Gilbert, E. A., Barclay, T., Schlieder, J. E., et al. 2020, *AJ*, **160**, 116
- Gilbert, E. A., Vanderburg, A., Rodriguez, J. E., et al. 2023, *ApJL*, **944**, L35
- Gillon, M., Jehin, E., Lederer, S. M., et al. 2016, *Natur*, **533**, 221
- Ginzburg, S., Schlichting, H. E., & Sari, R. 2018, *MNRAS*, **476**, 759
- Guerrero, N. M., Seager, S., Huang, C. X., et al. 2021, *ApJS*, **254**, 39
- Gupta, A., & Schlichting, H. E. 2019, *MNRAS*, **487**, 24
- Gupta, A., & Schlichting, H. E. 2020, *MNRAS*, **493**, 792
- Hamano, K., Abe, Y., & Genda, H. 2013, *Natur*, **497**, 607
- Hoffman, M. D., & Gelman, A. 2014, *JMLR*, **15**, 1593, <http://jmlr.org/papers/v15/hoffman14a.html>
- Howell, S. B., Sobeck, C., Haas, M., et al. 2014, *PASP*, **126**, 398
- Hunter, J. D. 2007, *CSE*, **9**, 90
- Inamdar, N. K., & Schlichting, H. E. 2015, *MNRAS*, **448**, 1751
- Jenkins, J. M., Twicken, J. D., McCauliff, S., et al. 2016, *Proc. SPIE*, **9913**, 99133E
- Jensen, E., 2013 Tapir: A web interface for transit/eclipse observability, Astrophysics Source Code Library, ascl:1306.007
- Jordan, S., Rimmer, P. B., Shorttle, O., & Constantinou, T. 2021, *ApJ*, **922**, 44
- Kane, S. R. 2022, *NatAs*, **6**, 420
- Kane, S. R., Arney, G., Crisp, D., et al. 2019, *JGRE*, **124**, 2015
- Kane, S. R., Barclay, T., & Gelino, D. M. 2013, *ApJL*, **770**, L20
- Kane, S. R., Ceja, A. Y., Way, M. J., & Quintana, E. V. 2018, *ApJ*, **869**, 46
- Kane, S. R., Kopparapu, R. K., & Domagal-Goldman, S. D. 2014, *ApJL*, **794**, L5
- Kane, S. R., Li, Z., Wolf, E. T., Ostberg, C., & Hill, M. L. 2021a, *AJ*, **161**, 31
- Kane, S. R., Arney, G. N., Byrne, P. K., et al. 2021b, *JGRE*, **126**, e06643
- Kane, S. R., Vervoort, P., Horner, J., & Pozuelos, F. J. 2020, *PSJ*, **1**, 42
- Kempton, E. M. R., Bean, J. L., Louie, D. R., et al. 2018, *PASP*, **130**, 114401
- Kesseli, A. Y., Kirkpatrick, J. D., Fajardo-Acosta, S. B., et al. 2019, *AJ*, **157**, 63
- Kipping, D. M. 2013, *MNRAS*, **435**, 2152
- Kluyver, T., Ragan-Kelley, B., & Pérez, F. 2016, in Positioning and Power in Academic Publishing: Players, Agents and Agendas, ed. F. Loizides & B. Schmidt (Amsterdam: IOS Press)
- Kopparapu, R. K., Ramirez, R., Kasting, J. F., et al. 2013, *ApJ*, **765**, 131
- Kopparapu, R. K., Ramirez, R. M., SchottelKotte, J., et al. 2014, *ApJL*, **787**, L29
- Kostov, V. B., Mullally, S. E., Quintana, E. V., et al. 2019, arXiv:1901.07459
- Krissansen-Totton, J., Fortney, J. J., & Nimmo, F. 2021, *PSJ*, **2**, 216
- Kumar, R., Carroll, C., Hartikainen, A., & Martin, O. A. 2019, *JOSS*, **4**, 1143
- Lee, E. J., & Connors, N. J. 2021, *ApJ*, **908**, 32
- Lee, E. J., Karalis, A., & Thormgren, D. P. 2022, arXiv:2201.09898
- Lightkurve Collaboration, Cardoso, J. V. d. M., Hedges, C., et al. 1812, Lightkurve: Kepler and TESS time series analysis in Python, Astrophysics Source Code Library, ascl:1812.013
- Lincowski, A. P., Lustig-Yaeger, J., & Meadows, V. S. 2019, *AJ*, **158**, 26
- Lincowski, A. P., Meadows, V. S., Crisp, D., et al. 2018, *ApJ*, **867**, 76
- Lissauer, J. J., Marcy, G. W., Rowe, J. F., et al. 2012, *ApJ*, **750**, 112
- Lithwick, Y., & Wu, Y. 2011, *ApJ*, **739**, 31
- Lopez, E. D., & Rice, K. 2018, *MNRAS*, **479**, 5303
- Louie, D. R., Deming, D., Albert, L., et al. 2018, *PASP*, **130**, 044401
- Luger, R., Agol, E., Foreman-Mackey, D., et al. 2019, *AJ*, **157**, 64
- Luque, R., & Pallé, E. 2022, *Sci*, **377**, 1211
- Lustig-Yaeger, J., Meadows, V. S., & Lincowski, A. P. 2019a, *ApJL*, **887**, L11
- Lustig-Yaeger, J., Meadows, V. S., & Lincowski, A. P. 2019b, *AJ*, **158**, 27
- Mann, A. W., Dupuy, T., Kraus, A. L., et al. 2019, *ApJ*, **871**, 63
- Mann, A. W., Feiden, G. A., Gaidos, E., Boyajian, T., & von Braun, K. 2015, *ApJ*, **804**, 64
- Margot, J.-L., Campbell, D. B., Giorgini, J. D., et al. 2021, *NatAs*, **5**, 676
- McKinney, W., et al. 2010, in Proc. of the 9th Python in Science Conf. 445 (Austin, TX: SciPy), 51
- Montet, B. T., Yee, J. C., & Penny, M. T. 2017, *PASP*, **129**, 044401
- Moran, S. E., Stevenson, K. B., Sing, D. K., et al. 2023, *ApJL*, **948**, L11
- Morton, T. D. 2012, *ApJ*, **761**, 6
- Morton, T. D., 2015 VESPA: False positive probabilities calculator, Astrophysics Source Code Library, ascl:1503.011
- Muirhead, P. S., Dressing, C. D., Mann, A. W., et al. 2018, *AJ*, **155**, 180
- Newton, E. R., Irwin, J., Charbonneau, D., et al. 2017, *ApJ*, **834**, 85
- Ostberg, C., & Kane, S. R. 2019, *AJ*, **158**, 195
- Ostberg, C., Kane, S. R., Li, Z., et al. 2023, *AJ*, **165**, 168
- Owen, J. E. 2017, *ApJ*, **847**, 29
- Owen, J. E., & Campos Estrada, B. 2020, *MNRAS*, **491**, 5287
- Owen, J. E., & Wu, Y. 2013, *ApJ*, **775**, 105
- Palubski, I. Z., Shields, A. L., & Deitrick, R. 2020, *ApJ*, **890**, 30
- Pecaut, M. J., & Mamajek, E. E. 2013, *ApJS*, **208**, 9
- Perez, F., & Granger, B. E. 2007, *CSE*, **9**, 21
- Popp, M., Schmidt, H., & Marotzke, J. 2016, *NatCo*, **7**, 10627
- Rackham, B. V., Apai, D., & Giampapa, M. S. 2018, *ApJ*, **853**, 122
- Ricker, G. R., Winn, J. N., Vanderspek, R., et al. 2015, *JATIS*, **1**, 014003
- Riello, M., De Angeli, F., Evans, D. W., et al. 2021, *A&A*, **649**, A3
- Rogers, J. G., Schlichting, H. E., & Owen, J. E. 2023, *ApJL*, **947**, L19
- Rowe, J. F., Bryson, S. T., Marcy, G. W., et al. 2014, *ApJ*, **784**, 45
- Safonov, B. S., Lysenko, P. A., & Dodin, A. V. 2017, *AstL*, **43**, 344
- Salvatier, J., Wiecki, T. V., & Fonnesbeck, C. 2016, *PeerJ Comp. Sci.*, **2**, e55
- Schaefer, L., & Fegley 2011, *ApJ*, **729**, 6
- Schlieder, J. E., Gonzales, E. J., Ciardi, D. R., et al. 2021, *FRASS*, **8**, 63
- Silverstein, M. L. 2019, PhD thesis, Georgia State University
- Skrutskie, M. F., Cutri, R. M., Stiening, R., et al. 2006, *AJ*, **131**, 1163
- Smith, J. C., Stumpe, M. C., Van Cleve, J. E., et al. 2012, *PASP*, **124**, 1000
- Smrekar, S., Hensley, S., Nybakken, R., et al. 2022, in IEEE Aerospace Conf. (AERO) (New York: IEEE), 1, <https://ieeexplore.ieee.org/document/9843269>
- Stassun, K. G., Oelkers, R. J., Paegert, M., et al. 2019, *AJ*, **158**, 138
- Stumpe, M. C., Smith, J. C., Catanzarite, J. H., et al. 2014, *PASP*, **126**, 100
- Stumpe, M. C., Smith, J. C., Van Cleve, J. E., et al. 2012, *PASP*, **124**, 985
- Suárez Mascareño, A., Rebolo, R., González Hernández, J. I., & Esposito, M. 2015, *MNRAS*, **452**, 2745
- Theano Development Team 2016, arXiv:1605.02688
- Turbet, M., Bolmont, E., Chaverot, G., et al. 2021, *Natur*, **598**, 276
- van der Walt, S., Colbert, S. C., & Varoquaux, G. 2011, *CSE*, **13**, 22
- Van Eylen, V., Agentoft, C., Lundkvist, M. S., et al. 2018, *MNRAS*, **479**, 4786
- Van Eylen, V., Albrecht, S., Huang, X., et al. 2019, *AJ*, **157**, 61
- Villanueva, G. L., Smith, M. D., Protopapa, S., Faggi, S., & Mandell, A. M. 2018, *JQSR*, **217**, 86
- Waalkes, W. C., Berta-Thompson, Z. K., Collins, K. A., et al. 2021, *AJ*, **161**, 13
- Way, M. J., & Del Genio, A. D. 2020, *JGRE*, **125**, e06276
- Way, M. J., Del Genio, A. D., Kiang, N. Y., et al. 2016, *GeoRL*, **43**, 8376
- Weiss, L. M., Millholland, S. C., Petigura, E. A., et al. 2022, arXiv:2203.10076
- West, A. A., Morgan, D. P., Bochanski, J. J., et al. 2011, *AJ*, **141**, 97
- Wizinowich, P., Acton, D. S., Shelton, C., et al. 2000, *PASP*, **112**, 315
- Wright, E. L., Eisenhardt, P. R. M., Mainzer, A. K., et al. 2010, *AJ*, **140**, 1868
- Zahnle, K. J., & Catling, D. C. 2017, *ApJ*, **843**, 122